Available online at www.sciencedirect.com
SCIENCE DIRECT®
Journal of Nuclear Materials 345 (2005) 206–218
journal of nuclear materials
www.elsevier.com/locate/jnucmat

Experimental determination of UO_2(cr) dissolution kinetics: Effects of solution saturation state and pH

E.M. Pierce [a,*], J.P. Icenhower [a], R.J. Serne [a], J.G. Catalano [b]

[a] *Applied Geology and Geochemistry Group, Environmental Technology Division, Pacific Northwest National Laboratory, P.O. Box 999 MS: K6-81, Richland, WA 99352, United States*
[b] *Department of Geological and Environmental Sciences, Stanford University, Stanford, CA 94305-2115, United States*

Received 12 November 2004; accepted 26 May 2005

Abstract

To evaluate the release of uranium from natural ore deposits, spent nuclear fuel repositories, and REDOX permeable reactive barriers (PRB), knowledge of the fundamental reaction kinetics associated with the dissolution of uranium dioxide is necessary. Dissolution of crystalline uranium (IV) dioxide under environmental conditions has been studied for four decades but a cardinal gap in the published literature is the effect of pH and solution saturation state on UO_2(cr) dissolution. To resolve inconsistencies, UO_2 dissolution experiments have been conducted under oxic conditions using the single-pass flow-through system. Experiments were conducted as a function of total dissolved carbonate ($[CO_3^{-3}]_T$) from 0.001 to 0.1 M; pH from 7.5 to 11.1; ratio of flow-through rate (q) to specific surface area (S), constant ionic strength (I) = 0.1 M, and temperatures (T) from 23 to 60 °C utilizing both powder and monolithic specimens. The results show that UO_2 dissolution varies as a function of the ratio q/S and temperature. At values of $\log_{10} q/S > -7.0$, UO_2 dissolution becomes invariant with respect to q/S, which can be interpreted as evidence for dissolution at the forward rate of reaction. The data collected in these experiments show the rate of UO_2 dissolution increased by an order of magnitude with a 30 °C increase in temperature. The results also show the overall dissolution rate increases with an increase in pH and decreases as the dissolved uranium concentration approaches saturation with respect to secondary reaction products. Thus, as the value of the reaction quotient, Q, approaches equilibrium, K, (with respect to a potential secondary phase) the dissolution rate decreases. This decrease in dissolution rate (r) was also observed when comparing measured UO_2 dissolution rates from static tests where $r = 1.7 \pm 0.14 \times 10^{-8}$ mol m^{-2} s^{-1} to the rate for flow-through reactors where $r = 3.1 \pm 1.2 \times 10^{-7}$ mol m^{-2} s^{-1}. Thus, using traditional static test methods can result in an underestimation of the true forward rate of UO_2(cr) dissolution. These results illustrate the importance of pH, solution saturation state, and the concentration of dissolved carbonate on the release of uranium from UO_2 in the natural environment.
Published by Elsevier B.V.

1. Introduction

REDOX permeable reactive subsurface barriers (e.g., chemically manipulated soils, microbial manipulated soils, and zero-valent iron) have been demonstrated to be effective in reducing and immobilizing redox-sensitive contaminants (i.e., chromium and uranium) in laboratory

* Corresponding author. Tel.: +1 509 376 2054.
E-mail address: eric.pierce@pnl.gov (E.M. Pierce).

0022-3115/$ - see front matter Published by Elsevier B.V.
doi:10.1016/j.jnucmat.2005.05.012

experiments [1–3] and field experiments [4–6]. Also, uranium reduction in laboratory experiments utilizing both biotic [2,7,8] and abiotic [1,9] permeable reactive barrier (PRB) techniques results in formation of a discrete UO_2 phase. Therefore, to predict the release of soluble uranium and the dissolution of uranium (IV) dioxide from natural ore deposits, spent nuclear fuel repositories, and REDOX permeable reactive barriers, knowledge of the fundamental reaction kinetics must be obtained.

More than four decades of past studies focusing on spent nuclear fuel disposal have quantified the kinetics of UO_2(cr) dissolution [10–23], but the findings, although important, reveal significant gaps in the quantitative understanding of UO_2(cr) reactivity. For a comprehensive discussion of previous results, the reader should consult the review papers by Grambow [24] and Shoesmith [25]. These reviews have identified two factors that have contributed to the uncertainty in dissolution rates, (1) solution saturation state and (2) pH. Therefore, the focus of this study was to determine the effect of pH and solution saturation state in the presence of carbonate on the oxidative dissolution of a crystalline form of uranium (IV) oxide [UO_2(cr)] as a model solid.

Our first concern was that several previous experimental investigations of UO_2 reactivity were conducted using a static reactor (e.g., batch reactor) rather than more applicable flow-through reactors [10–16,19]. Dissolution rates cannot be evaluated accurately under conditions of both near-saturation and dilute dissolved uranium concentrations using the traditional static reactor.

Second, numerous studies have been conducted to evaluate the effect of pH (3.0–11.0) on the dissolution of UO_2 under oxidizing and reducing conditions [11,13–15,17,22,26]. All investigators have observed a linear relationship of pH on the dissolution rate from the acidic to near neutral range (i.e., from pH = 3.0 to 6.8) and a dissolution rate that becomes insensitive to pH from the near neutral to alkaline range (i.e., from pH = 6.8 to 11.0). The scatter shown in the data obtained by Torrero et al. [22] under oxidizing conditions and at pH values greater than 6.8 was attributed to the formation of a partially oxidized surface layer. Other investigators [22,27] have also observed the formation of a partially oxidized surface film within this pH range (e.g., from 7 to 11), when evaluating the dissolution of UO_2 under oxidized conditions with a total dissolved carbonate concentration ($[CO_3^{2-}]_T$) less than 10^{-3} M. The formation of this surface film has led to the conclusion that UO_2 dissolution is insensitive to pH within this range.

The X-ray photoelectron spectroscopy (XPS) results presented by Casas et al. [18] and Torrero et al. [22] suggested the surface film had a U/O ratio similar to $UO_{2.25}$ (e.g., U_4O_9). Previous experiments [12,27–30], in the absence of bicarbonate, illustrated that this surface film formed numerous intermediate uranium phases over time resulting in a final composition of $UO_3 \cdot xH_2O$(cr). The apparent mechanism for the formation of this oxidized surface film is slow detachment of the oxidized metal species from the surface of the UO_2 crystal lattice. In the presence of a total dissolved carbonate concentration of 10^{-3} M or greater, strong aqueous uranyl carbonate complexes prevent the formation of this surface layer, allowing an investigator to evaluate the reactivity of the pure UO_2 surface within the near neutral to alkaline pH range. The inhibitive effect of high carbonate concentrations on formation of the oxidized surface film was proven by the XPS results of Pablo et al. [23].

Pablo et al. [23] investigated the effects of $[CO_3^{2-}]_T$ on the reactivity of UO_2(cr) at a pH of 8.0 as a function of temperature (from 10 to 60 °C) and $[CO_3^{2-}]_T$ (from 10^{-4} to $10^{-1.5}$ M). In this investigation, Pablo et al. [23] confirmed by XPS that a surface film was not detected. They attribute the lack of the surface film to the complexation of surface oxidized uranium with dissolved carbonate and subsequent transport of the $U^{VI} - HCO_3^-$ complex into solution. They propose several step-wise mechanisms for this process that begin with UO_2 surface oxidation, then uranium surface coordination and complexation with the bicarbonate ion, and finally detachment of the uranyl–carbonate complex into solution. Although the results obtained by Pablo et al. [23] provide critical information on the mechanisms of UO_2 dissolution, other factors that affect uranium dissolution, such as the effect of the solution saturation state and pH, were not addressed and thus merit investigation.

The purpose of this study was to determine the dissolution kinetics of UO_2(cr) in the presence of atmospheric oxygen as a function of temperature, solution saturation state, and pH. Accordingly, the principal objective was to determine the dissolution rates over a large flow-rate-to-surface-area interval to examine the effects of solution saturation state. Examining the dissolution process of UO_2(cr) as a function of these variables provides information on the rates near and far from saturation with respect to potential secondary phases. These and other factors will affect the release of uranium from natural and repository environments; as well as subsurface REDOX permeable reactive barriers, once oxidizing conditions prevail.

2. Experimental details

2.1. Sample preparation

Commercially available crystalline uranium(IV) dioxide (UO_2) was obtained from Alfa Aeasar® as a powdered specimen containing an average particle diameter of 213 μm. The UO_2 sample was calcined at approximately 900 °C using a Lindberg™ furnace in a reducing atmosphere of 92% argon and 8% hydrogen to remove any surface oxidation. Once calcined, the UO_2 sample

was stored under an inert nitrogen (N_2) atmosphere inside a Lab-Conco® atmospheric chamber. Both powder and monolith specimens were used to evaluate UO_2 dissolution.

The calcined UO_2 was ground inside the controlled N_2 chamber using an agate mortar/pestle and dry-sieved into the desired size fractions using ASTM procedure ASTM C136 [31]. The desired size fractions for the powder specimens had average diameters of 36.5 μm, 89.5 μm, 141 μm, and 213.5 μm. Particles with an average diameter less than 74 μm were used to fabricate UO_2 monoliths.

The UO_2 monoliths, with an average weight of 2 g, were made using a Carver™ press by applying a pressure of 3500 lb in a cell with an average diameter of 1.02 cm. Each calcined monolith had the following dimensions, measured using a Vernier caliper: an average diameter of 1.02 cm and thickness of 0.23 cm. The densities of these monoliths were measured using a Micromeritics AccuPyc® 1330 gas pycnometer. Results indicated these UO_2 monoliths had an average density of 10.36 g/cm^3, which is 94.5% of the theoretical density (e.g., 10.96 g/cm^3). After fabrication the monoliths were calcined and stored under the same inert atmosphere as the powder specimens.

2.2. Characterization

The UO_2 powder diffraction pattern for the calcined powders was collected using a Scintag® automated powder diffractometer (Model 3520) with CuK_α radiation X-ray tube ($\lambda = 1.54$ Å). The sample was analyzed using a 2θ range from 2° to 65°, a step size of 0.01°, and a 9 s count time at each step. Before mounting, a representative sample of the bulk material was ground using an agate mortar and pestle in the atmospheric chamber and sealed in a specialized XRD holder to minimize oxidation [32]. In addition to XRD, a nitric acid (HNO_3) chemical digestion method was used to determine the bulk elemental composition of the calcined crystalline uranium (IV) dioxide sample. A 0.20 g grab sample was dissolved in 20 mL of 8 M HNO_3, analyzed for trace metals utilizing inductively couple plasma optical emission spectroscopy (ICP-OES) and uranium utilizing kinetic phosphorescence analysis (KPA model-11).

The morphology and size of calcined UO_2 powder and monolith specimens were determined with a JEOL JSM-840 scanning electron microscope (SEM). The system is equipped with an Oxford Links ISIS 300 energy dispersive X-ray analysis (EDS) system that was used for qualitative elemental analysis. Operating conditions consisted of 20 keV for SEM imaging, 100 live seconds with 20–30% dead time for the EDS analyses. The EDS analyses of particles are limited to elements with atomic weights heavier than boron. Photomicrographs of high-resolution secondary electron images were obtained as digital images and stored in electronic format. The SEM/EDS mounts consisted of double-sided carbon tape attached to standard aluminum mounting stubs. After initial optical inspection, the sample mount was coated with carbon using a vacuum sputter coater to improve the conductivity of the samples and quality of the SEM images and EDS signals.

2.3. X-ray absorption spectroscopy

Uranium L_{III}-edge X-ray absorption fine structure (XAFS) measurements were performed on the calcined UO_2 sample to verify its identity and evaluate the oxidation state of the initial material. XAFS is an element-specific, short-range structural probe that provides information on the local structure and composition of the element of interest [33]. The X-ray absorption near-edge structure (XANES) region of the spectrum provides information about the oxidation state and local coordination environment of the element, whereas the extended X-ray absorption fine structure (EXAFS) region provides information on the type, distance to, and number of neighboring atoms.

The uranium L_{III}-edge XAFS measurements of the UO_2 sample were conducted at room temperature on the Molecular Environmental Sciences beam line 11-2 [34] at the Stanford Synchrotron Radiation Laboratory (SSRL) using cryogenically cooled Si(220), $\phi = 90°$ double-crystal monochromator. Fluorescence yield data were collected using an argon-filled Stern-Heald type detector [35]. A collimating mirror placed in front of the monochromator was used for harmonic rejection, with a cutoff of 22 keV. A yttrium metal foil was mounted between two ionization chambers downstream of the sample for energy calibration; the first inflection point in the yttrium *K*-edge was set to 17038 eV. The uranium L_{III}-edge XAFS measurements of the UO_2 and schoepite standards were measured in transmission mode at SSRL on beam line 4-3 using a Si(220), $\phi = 0°$ double-crystal monochromator.

XAFS data were processed using the computer code SixPACK [36] interface to IFEFFIT [37]. XANES data were background-subtracted and normalized to an edge-step of one. After background-subtraction, the EXAFS data were extracted and K^3-weighted. Phase shift and backscattering amplitude functions for quantitative EXAFS fitting were generated from the crystal structure of UO_2 [38] using the computer code FEFF 7 [39].

2.4. SPFT experiments

Dissolution experiments were conducted using the single pass flow-through (SPFT) apparatus. A general description of the SPFT system is provided in this section. For a more detailed discussion of the SPFT system and the advantages for using the SPFT system instead of

other techniques, see [40–43] as well as the references contained therein.

All SPFT experiments were conducted in triplicate and started by injecting sodium bicarbonate ($NaHCO_3$) solutions (from 10^{-3} to 10^{-1} M) into the system at flow-through rates ranging from 6 to 120 mL d^{-1} (from ~0.1 to 2 reactor volumes per day) using a Kloehn™ syringe pump. Each reactor was wrapped in polyurethane insulation and immersed in a 5.7-L low-temperature custom-designed oven (LTCDO). The LTCDO was lined with 4-mm soda lime glass beads to aid in heat transfer. A C3390-Omega temperature controller was used to control the LTCDO temperature by interrupting the electrical current in an on/off fashion. The solution temperatures inside the reactors were measured using in situ thermocouples. Flow rates were determined gravimetrically at each sampling time. Flow-rate variations were typically less than 5%. Once steady-state test conditions (i.e., buffers, flow rates, temperatures, etc.) were established, the pre-weighed UO_2(cr) samples [e.g., powder (~0.5 g) or monoliths (~2 g)] were removed from the atmospheric chamber in sealed vials and placed into each preheated test reactor. Experiments were run until steady-state effluent solution conditions prevailed, which required approximately 7–42 days, depending on the flow rate or the time necessary to exchange seven or more reactor volumes.

2.5. Static experiments

Static replenishment experiments (i.e., batch test) were conducted in triplicate and began by placing 60 mL of 0.1 M $NaHCO_3$ solution into a Savillex™ Teflon® reactor and heating the reactor to 60 °C. Once the test conditions were established, 0.5 g of the calcined UO_2(cr) powder was added. Solution samples from each experiment were collected in 5-mL increments using a calibrated 5-mL pipette. Each reactor was sampled by removing a 5-mL aliquot, placing the aliquot into a tared scintillation vial, and replenishing the reactor with a 5-mL aliquot of new 0.1 M $NaHCO_3$ solution. These experiments were allowed to continue until a steady-state condition was achieved, occurring between the eleventh and twenty-fifth day of testing.

2.6. Solution composition and geochemical modeling

Dissolved uranium concentrations were determined using a kinetic phosphorescence analyzer (KPA) [44] and/or inductively coupled plasma mass spectrometry (ICP-MS). Concentrations of $[CO_3^{2-}]_T$ in the effluent solutions were measured by ion chromatography (IC) and titrimetric techniques.

Although the effluent solution pH was monitored, the in situ pH was calculated for each test temperature using EQ3NR [45]; the results are given in Table 1. It is important to take into account the change in pH that occurs at different temperatures when computing dissolution rates from SPFT data because the in situ pH can vary by as much as 0.2 pH units over the temperature range from 23 to 90 °C.

2.7. Measurement of the dissolution rates

Based on thermodynamic modeling of the experimental conditions using EQ3NR [45], the uranyl tri-carbonate species, $UO_2(CO_3)_3^{4-}$, was predicted to be the predominant uranium species in the test effluent solutions, as illustrated in Eq. (1).

$$UO_2(cr) + (1/2)O_2 + 3HCO_3^- \rightarrow UO_2(CO_3)_3^{4-} + H_2O + H^+ \quad (1)$$

The dissolution rates (r), which are based on steady-state uranium concentrations in the effluent, were normalized against the average background uranium concentration using Eq. (2), where r is the dissolution rate of element i (mol m^{-2} s^{-1}), C_i is the effluent concentration of element i (mol L^{-1}), $\bar{C}_{i,b}$ is the average

Table 1
Composition of solutions used in SPFT experiments

Soln. #	Composition	pH @			
		23 °C	30 °C	60 °C	90 °C
1	0.1 M $NaHCO_3$ + 0.0046 M HNO_3	7.5	7.4	n.d.*	n.d.
2	0.1 M $NaHCO_3$ + 0.00071 M HNO_3	8.0	7.9	7.8	7.8
3	0.1 M $NaHCO_3$ + 0.024 M NaOH	9.7	9.3	n.d.	n.d.
4	0.1 M $NaHCO_3$ + 0.099 M NaOH	11.2	11.1	n.d.	n.d.
5	0.05 M $NaHCO_3$ + 0.05 M NaCl + 0.00035 M HNO_3	8.0	7.9	n.d.	n.d.
6	0.001 M $NaHCO_3$ + 0.099 M NaCl + 0.0000057 M HNO_3	8.0	7.9	n.d.	n.d.

Solution pH values above 23 °C were calculated with EQ3NR Code V7.2b database.
Soln.# – refers to solution number.
* n.d. Corresponds to the experiments that were not conducted.

background concentration of element i (mol L^{-1}), q is the flow rate (L s^{-1}), and S is the surface area of the sample (m^2).

$$\text{Dissolution rate } r_i = \frac{(C_i - \bar{C}_{i,b})q}{S}. \quad (2)$$

The experimental uncertainty was determined using Eq. (3), which considers the propagation of random errors [46]. McGrail et al. [43] illustrated that the experimental uncertainty associated with the dissolution rate can be determined by accounting for the uncertainties associated with each parameter in Eq. (2). For uncorrelated random errors, the standard deviation of a function $f(x_1, x_2, \ldots, x_n)$ is given by

$$\sigma_f = \sqrt{\sum_{i=1}^{n} \left(\frac{\partial f}{\partial x_i}\right)^2 \sigma_i^2}, \quad (3)$$

where σ_f = standard deviation of the function f, x_i = parameter i, and σ_i = standard deviation of parameter i. By substituting Eq. (2) into Eq. (3), and expressing Eq. (3) in terms of relative errors, Eq. (4), results.

$$\hat{\sigma}_{r_i} = \sqrt{\frac{(\hat{\sigma}_{C_i} C_i)^2 + (\hat{\sigma}_{\bar{C}_{i,b}} \bar{C}_{i,b})^2}{(C_i - \bar{C}_{i,b})^2} + \hat{\sigma}_q^2 + \hat{\sigma}_S^2}, \quad (4)$$

where $\hat{\sigma}_{r_i} = \sigma_{r_i}/r_i$. Relative errors of 10%, 10%, 5%, and 15% for C_i, $\bar{C}_{i,b}$, q, and S, respectively, are typical for these measurements. Conservative appraisal of errors was assigned to the parameters in Eq. (3) in addition to imputing detection threshold values for background concentrations, resulting in a 2σ uncertainty of approximately ±35% in the dissolution rate.

3. Results and discussion

3.1. XRD, chemical digestion, and BET results

X-ray diffraction results confirmed the calcined UO_2 samples used in this study were consistent with published spectra of UO_2 (Powder Diffraction File [PDF] # 41-1422). A comparison between these two patterns showed the correct 100%, 50%, 50%, 45%, and 8% relative intensity peaks at 28.2°, 32.7°, 46.7°, 55.8°, and 58.4° 2θ, respectively. The chemical digestion and BET results suggest the UO_2 sample was 99.9% pure and had Kr-adsorption surface area of 1.2 $m^2\ g^{-1}$.

3.2. XANES results

The XANES spectrum of the UO_2 sample (Fig. 1) is consistent with published spectra of UO_2 [47–49]. The edge position, based on both the main peak position in the XANES spectrum and the first peak position in the first derivative XANES spectrum, are correct for UO_2, and about 4 eV lower than that of U(VI) mineral schoepite, $[(UO_2)_8O_2(OH)_{12} \cdot 12H_2O]$. In addition, the UO_2 sample lacks the strong resonant feature of the U(VI) compound located at roughly 17 190 eV. This shoulder is due to the presence of the uranyl moiety, UO_2^{2+} [48,49]. There is no indication of the presence of any oxidized uranium in the sample, although XANES is not sensitive to small quantities of U(VI), (i.e., <10%) [50].

3.3. EXAFS results

The EXAFS spectrum of the UO_2 sample is nearly identical to that of a UO_2 standard (Fig. 2). The Fourier

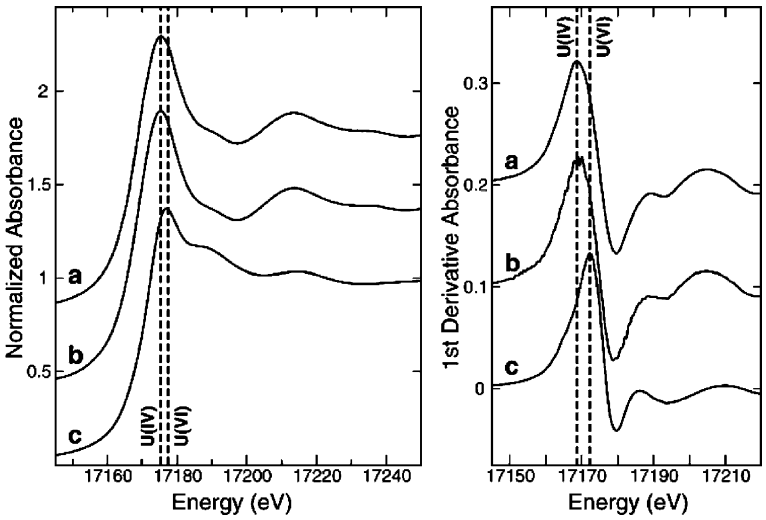

Fig. 1. XANES (left) and first derivative XANES (right) spectra of (a) UO_2 standard, (b) UO_2 sample, and (c) schoepite, a U(VI) standard.

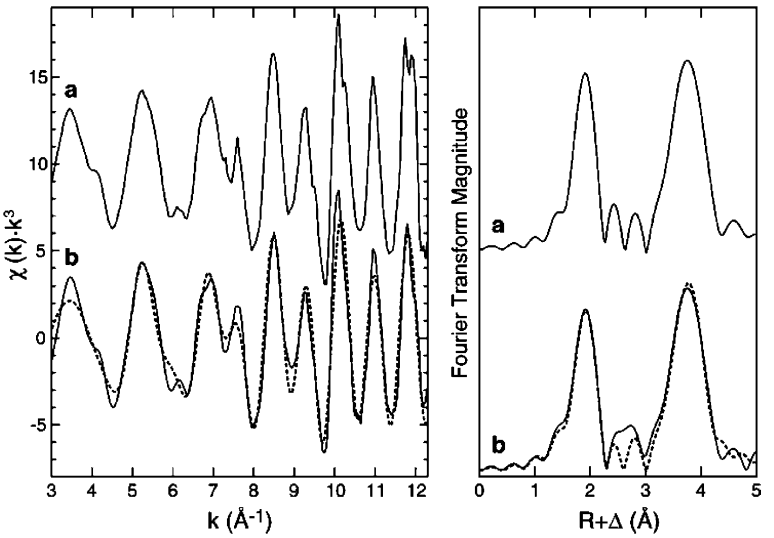

Fig. 2. EXAFS (left) and Fourier transform (right) spectra of (a) UO_2 standard, and (b) UO_2 sample. The dashed line is the best fit to the EXAFS spectrum of the UO_2 sample.

Table 2
EXAFS fitting results, including coordination number (N), interatomic distance (R), and Debye-Waller-type factor (σ^2), compared to the structural parameters of UO_2 from the crystal structure provided in Wasserstein [38]

Shell	N	R (Å)	σ^2 (10^{-3}Å^2)
Best fit to data			
U-O1	8[a]	2.35 ± 0.02	6 ± 1
U-U	12[a]	3.86 ± 0.02	5 ± 1
U-O2	24[a]	4.49 ± 0.04	9 ± 6
Crystal structure			
U-O1	8	2.36	
U-U	12	3.85	
U-O2	24	4.51	

[a] Value held constant during fitting.

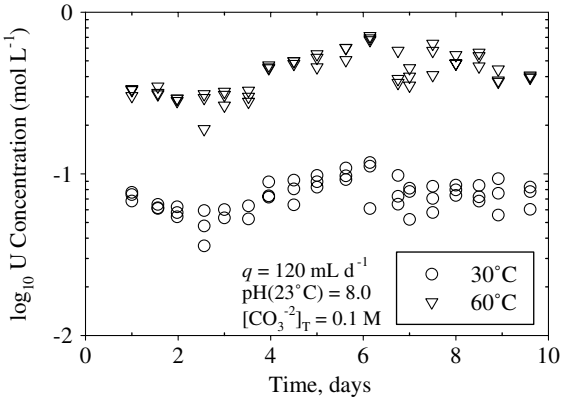

Fig. 3. U concentration, in mol L^{-1}, as a function of time at 30 °C (circles) and 60 °C (triangles). Experiments conducted using the calcined UO_2(cr) powder specimens.

transforms of the EXAFS spectra of both the sample and the standard have two large peaks corresponding to the first three atomic shells (U-O1, U-U, and U-O2) surrounding the U atom in UO_2. The inter-atomic distances obtained from fitting a structural model to the EXAFS spectrum of the UO_2 sample (Table 2) are consistent with the structure of UO_2. There is no evidence for the presence of U(VI) in the sample as a large Fourier transform peak at ~1.4 Å is not observed.

3.4. SPFT results

The measured uranium concentrations in the effluent attain steady-state rapidly and become invariant with respect to time after approximately 6 days at a flow rate of 120 mL d^{-1} and 60 °C (Fig. 3). A transient effect, manifest as an initial rapid release (i.e., pulse) of U, was not observed in tests using calcined material (Fig. 3), in comparison to tests conducted with as received UO_2 (Fig. 4). This transient effect, followed by a slow decrease in U concentration until steady-state was achieved, has been observed by previous investigators [18,26] and is caused by samples containing some amount of an oxidized U^{VI} oxide coating, which was confirmed by XRD. The XRD pattern of the as-received grains revealed an uncharacteristic UO_2 peak at 17° 2θ, which appears to be a peak associated with uranyl oxide, such as schoepite ($UO_3 \cdot xH_2O$). Most uranyl oxides possess a signature peak between 10° and 17° 2θ [51]. Thus, the process of calcining this material apparently removed any oxidation and

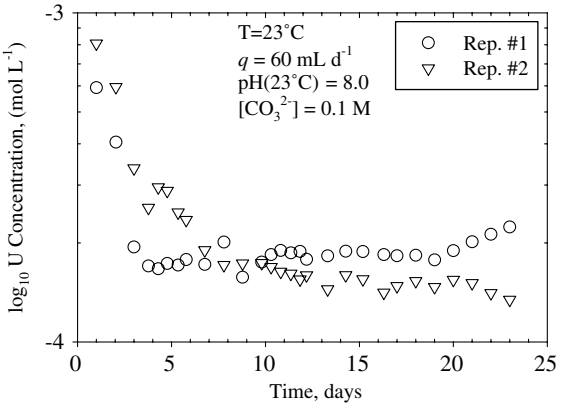

Fig. 4. U concentration, in mol L^{-1}, as a function of time for the pre-calcined UO_2 at 23 °C. Experiments conducted using the as received UO_2(cr) powder specimens.

suggests that pretreatment of the UO_2 solid is necessary to remove oxidized coatings. The presence of this oxidized surface layer can also be attributed to the observed difference in the measured steady-state U concentration between the calcined (Fig. 3) and as received (Fig. 4) UO_2 particles in these experiments.

The uranium concentration in the effluents increased by 0.4–0.7 $\log_{10}$ units with a 30 °C increase in temperature (Fig. 3). Also, the $\log_{10}$U concentration (mol L^{-1}) decreased with increasing flow rate. The decrease in uranium concentration as a function of flow rate was a result of the solution residence time. The effluent uranium concentration will increase with an increase in solid to solution contact time until saturation is achieved, with respect to a potential secondary uranium phase. Therefore, before using the steady-state uranium concentrations to compute the UO_2 dissolution rate, it must be demonstrated the formation of secondary phases did not significantly alter the measured solution concentration of uranium.

3.5. Geochemical modeling of the solution composition

Geochemical modeling using EQ3NR [45] was used to evaluate the aqueous speciation and saturation state of the effluent solutions with respect to key uranyl minerals and aqueous species using an updated thermodynamic database. The $\log_{10}$ equilibrium constants (K) for all minerals and aqueous species are based on either measured or estimated free energy values from various literature sources [52–63].

Applying geochemical modeling to the steady-state uranium concentrations measured in each experiment provided insight into the uranium solution speciation within the SPFT reactor. For solution conditions ranging from 0.1 to 0.05 M $[CO_3^{2-}]_T$, and at pH (23 °C) from 8.0 to 11.1, the modeling calculations predicted that greater than 99.3% of the total dissolved uranium would be composed of the uranyl tri-carbonate $[UO_2(CO_3)_3^{4-}]$ aqueous species. A decrease in pH by 0.5 units (e.g., pH = 7.5) at a $[CO_3^{2-}]_T = 0.1$ M, resulted in a uranium species distribution of 98.6% $UO_2(CO_3)_3^{4-}$ with the remaining 1.4% as uranyl di-carbonate $[UO_2(CO_3)_2^{2-}]$ aqueous species. Decreasing the total dissolved carbonate concentration by two orders of magnitude ($[CO_3^{2-}]_T = 0.001$) caused major changes in uranium solution speciation. Although $UO_2(CO_3)_3^{4-}$ (66.7%) was still the dominant uranium solution species at $[CO_3^{2-}]_T = 0.001$ M and pH = 8.0, other aqueous-uranyl carbonate species became significant [e.g., $UO_2(CO_3)_2^{2-}$ = 28.1%].

Aqueous speciation and saturation indices calculated from the solution chemistry data suggest that effluent solutions were under-saturated with respect to potential secondary phases at steady-state conditions. The geochemistry of uranium is complicated. There are considerable differences or uncertainties in the stoichiometry and thermodynamic values assigned to uranium secondary minerals, especially those exhibiting complex and variable compositions [62]. Therefore, solubility calculations based on the current knowledge of these values may have significant uncertainty and should be considered semi-quantitative.

3.6. Effect of solution saturation state and surface area

Experiments over a range of the ratio of flow-rate (q)-to-surface area (S) were conducted in an attempt to identify the forward (or maximum) dissolution rate. The $\log_{10}$ dissolution rates (mol m^{-2} s^{-1}) based on the steady-state concentration of uranium were plotted for the measurements conducted at 60 °C, pH = 8.0, and $[CO_3^{2-}]_T = 0.1$ M (Fig. 5). By varying the ratio of flow-through rate, q, to sample surface area, S, the

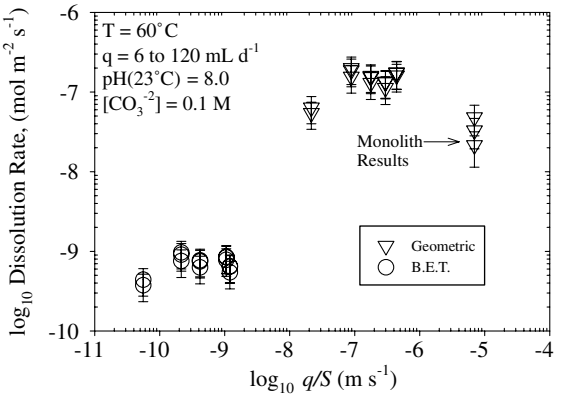

Fig. 5. A plot of the forward rate of dissolution, comparing the calculated geometric surface area to the measured Kr-adsorption BET.

dissolution rate reached a maximum at $\log_{10}(q/S)$ greater than −7.0 at 60 °C (Fig. 5), for the powdered specimens. The $\log_{10}$ dissolution rates increased to a maximum, $\log_{10}(q/S)$ of −7.0, and thereafter remained constant within experimental error. This plateau is commonly referred to as the forward or maximum dissolution rate. The data shown at a $\log_{10}(q/S)$ of −5.2, see Fig. 5, correspond to the experiments conducted using UO_2 monoliths and are addressed later in this section.

The dissolution rate decreased with decreasing q/S because when flow-rates were low or total surface area was high, the concentrations of elements dissolved into solution were high. As the concentration of uranium increased in solution, the solution approached saturation with respect to potential secondary phases (Fig. 6). Therefore, the dissolution rate slowed as the chemical potential between UO_2 and the solution decreased. This effect can be expressed mathematically as the chemical affinity of reaction, Eq. (5)

$$A = RT \ln\left(\frac{K}{Q}\right) = -\Delta G_r, \tag{5}$$

where A is the chemical affinity, ΔG_r is the free energy of reaction (kJ mol^{-1}), R is the gas constant (J mol^{-1} K^{-1}), T is the temperature (K), K is the equilibrium constant, and Q is the ion activity product [64]. Chemical affinity is a measure of the departure from equilibrium. As the ion activity product, Q, approaches the value of the equilibrium constant, K, the chemical affinity term goes to zero. Consequently, to evaluate the effects of various environmental factors (i.e., temperature, pH, and bicarbonate activity) on the dissolution of UO_2, the solution saturation state must be known.

Fig. 5 also illustrates that with powder specimens, the method used to determine the surface area of a sample can result in a one to two order of magnitude difference in the calculated dissolution rate. In an attempt to determine which surface area measurement was more applicable, dissolution experiments using sintered monoliths were conducted and compared to the powder results. The geometric surface area for the powder specimens were computed using Eq. (6),

$$S_{GEO} = \left(\frac{3m}{\rho r}\right), \tag{6}$$

where S_{GEO} is the specific surface area, ρ is the particle density (~10.96 g cm^{-3}), r is the average radius (cm), and m is the sample mass (g). This formula assumes the particles are spherical, size distributions of the grains are normally distributed, and that surface pits, cracks, and other forms of surface roughness do not significantly increase the surface area. The particles used in these experiments have a spherical morphology and the size distribution appears to be normally distributed, evident by the SEM images of the pre- and post-test UO_2 grains. These results suggest that two of the three assumptions used to determine the geometric surface area are satisfied.

Dissolution rates for powdered specimens, computed using the geometric surface area, were slightly higher than the dissolution rates for sintered monoliths and may be the result of the increased reactivity that occurs when conducting these experiments with powder specimens. This correlation between powder and monolith results, when normalized using the geometric surface area, suggests the geometric surface area provides a better estimate of the reactive surface area for powder samples than does the measured BET surface area. Therefore, all rates computed in this study were normalized using the geometric surface area. Observed differences in rates computed using either the geometric or BET surface area have been previously reported for UO_2 [20,21] as well as for silicate minerals, and may be the result of surface roughness. Surface roughness is defined as the ratio of the BET specific surface area to the geometric surface area [65]. For the powdered specimens used in this

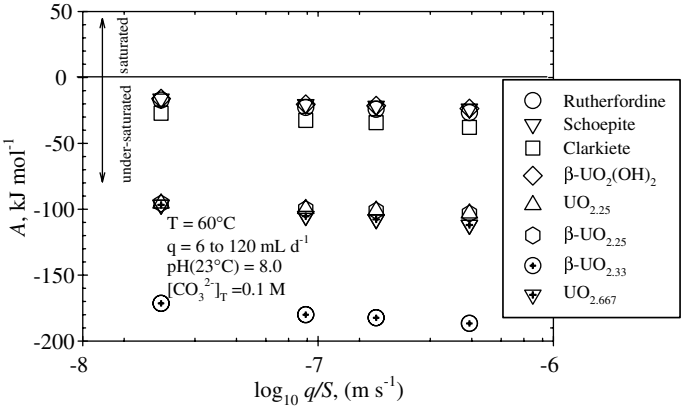

Fig. 6. Chemical affinity of potential U secondary phases as a function of $\log_{10} q/S$.

study, the surface roughness factor was an order of magnitude greater than the value reported by Gray and Wilson [21].

Other factors that complicate the estimate of specific surface area are the changes each sample undergoes during the dissolution experiment, where specific surface area increases with increasing time. By using Eqs. (7) and (8) from McGrail et al. [66]:

$$S_i = \left(\frac{3}{\rho r}\right) m_0^{1/3} m_i^{2/3}, \tag{7}$$

$$m_i = m_0 - \frac{1}{f_k}\left[\sum_{j=1}^{i-1} q_j C_{j,k} \Delta t_j + q_i C_{i,k} \frac{\Delta t_i}{2}\right], \quad i \geqslant 1, \tag{8}$$

where m_0 is initial mass, m_i is mass at time i, f_k is mass fraction of element k, $C_{j,k}$ is the concentration of element k at time j or i, q is the flow rate at time j or i, and Δt is the change in time, the change in surface area over time was computed. For additional details on Eqs. (7) and (8), the reader should consult McGrail et al. [66].

Fig. 7 illustrates that as the temperature increased the effect of surface area changes on the dissolution rate also increased. These results indicate the evaluation of UO_2 reactivity (i.e., UO_2 dissolution rate) using powder specimens as a function of temperature, requires that time-dependent surface area changes be used during the course of the experiment. For the 30 and 60 °C powder experiments, a mass loss ranging from 7% to 35% was calculated in several tests.

3.7. Effect of pH

To determine the effect of pH on the dissolution rate, solution pH values were varied from 7.5 to 11.1 at 30 °C and $[CO_3^{2-}]_T$ at 0.1 M. The in situ solution pH was corrected for the temperature effect using EQ3NR [45] (Table 1).

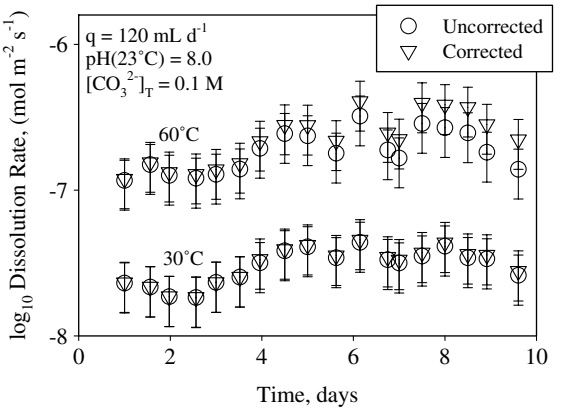

Fig. 7. Dissolution rate calculated using the corrected (triangles) vs. uncorrected (circles) geometric surface area at 30 °C and 60 °C.

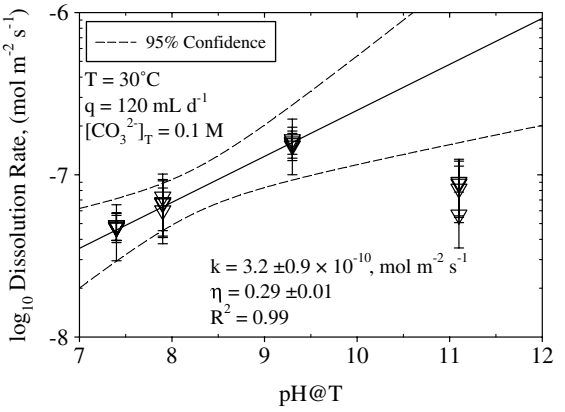

Fig. 8. Dissolution rate as a function of pH.

Fig. 8 illustrates that as pH increased, the overall UO_2 dissolution rate also increased until near-saturated conditions were approached (near pH 11.1) with respect to a potential uranyl solid phase. Geochemical modeling of the measured solution chemistry suggests that experiments at pH 11.1 are approaching saturation with respect to clarkeite [$Na_2U_2O_7$ (cr)], with a corresponding solution chemical affinity of $A = -10.2\ \mathrm{kJ\,mol^{-1}}$ (Fig. 9). Although the affinity term suggests these solutions are under-saturated, in dynamic experiments such as these, the amorphous analog usually forms earlier than the crystalline phase. These thermodynamic calculations are based on the solubility product (K_{sp}) for the crystalline parent, which is always lower than that of the amorphous analog.

$$r_i = k_0 (a_i)^{\eta_i}. \tag{9}$$

Using Eq. (9), where r_i = dissolution rate (mol m^{-2} s^{-1}), k_0 is the intrinsic rate constant (m s^{-1}), a is the activity of any specie i (mol L^{-1}), and η is the power law coefficient (i.e., reaction order) for any species i, a non-linear regression was performed over the entire data set, excluding the results at pH 11.1. The resulting regression coefficients are $k_0 = 3.2 \pm 0.9 \times 10^{-10}$ (mol m^{-2} s^{-1}) and $\eta_{pH} = 0.29 \pm 0.01$ with a correlation coefficient (R^2) of 0.99.

These results show that, in the presence of carbonate, pH affects the dissolution of UO_2 by enhancing the solubility of the oxidized surface film. At pH 8.0 and 30 °C the observed rate was two to three orders of magnitude greater than the rate reported by Torrero et al. [22] (3.1×10^{-11} mol m^{-2} s^{-1}), measured at 25 °C, pH 8.8, and 21% O_2 in a 0.01 M solution of sodium perchlorate ($NaClO_4$). Thermodynamic modeling of their steady-state solution chemistry suggests that the concentration of dissolved U was approaching saturation with respect to a secondary uranyl oxide, possibly $UO_3 \cdot xH_2O$, with a corresponding $A = -11.9$ kJ mol^{-1}.

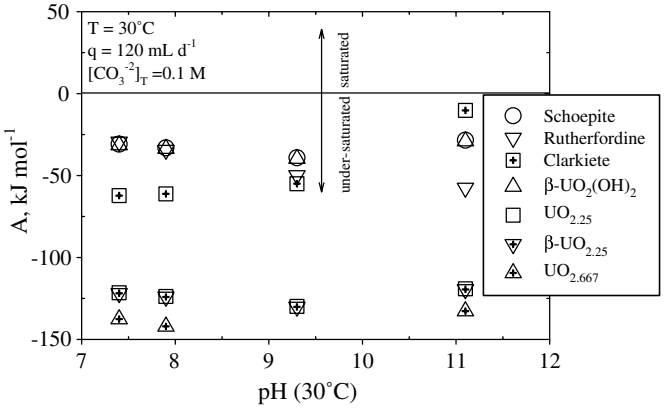

Fig. 9. Chemical affinity of potential U secondary phases as a function of pH.

By combining the results shown in Fig. 8 with the results observed by Torrero et al. [22], we concluded that from the acidic to alkaline pH range, the UO_2 dissolution rate first decreased, reached a minimum around pH 6, and then increased with increasing pH. This observed increase within the neutral to alkaline pH range was due to the complexation of the oxidized U species with bicarbonate. Although additional information is needed to determine the step-wise mechanism and the rate-limiting step in the dissolution reaction, it is clear from these results the proposed mechanism by Pablo et al. [23] must include the effect of pH on the dissolution rate.

3.8. Comparison of static replenishment tests

To provide additional information on the factors that have contributed to the uncertainty in UO_2 dissolution rates collected by previous investigators, static replenishment experiments were conducted and compared to the results of flow-through experiments.

Fig. 10 illustrates that from the eleventh through the twenty-fifth day the uranium concentrations become invariant with respect to time, and confirms that these experiments have attained steady state. Based on these results, the values of normalized mass loss of uranium were computed for the static tests conducted at 60 °C in $[CO_3^{2-}]_T$ of 0.1 M at pH 8.0 and are plotted as a function of time (Fig. 11). The slope of the line provides the average normalized release rate (g m^{-2} d^{-1}) and was determined by conducting a linear regression on the results obtained from the eleventh through twenty-fifth day. The regressed average normalized release rate of $1.7 \pm 0.14 \times 10^{-8}$ mol m^{-2} s^{-1} was not within the experimental error of the maximum release rate computed from the SPFT data at 60 °C in $[CO_3^{2-}]_T$ of 0.1 M at pH 8.0 and $q = 120$ mL d^{-1} (i.e., $1 \pm 1.2 \times 10^{-7}$ mol m^{-2} s^{-1}). For this set of static experiments, a linear regression of the uranium release data produced a large uncertainty in the dissolution rate. These uncertainties were caused by large progressive changes in chemical affinity during the static test. As the concentration of U in solution increased

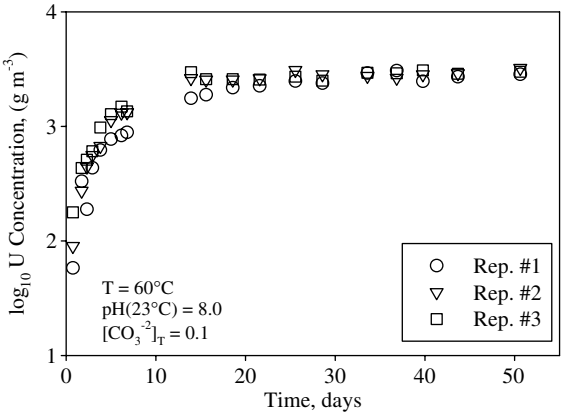

Fig. 10. $Log_{10}[U]$ vs. time for static experiments.

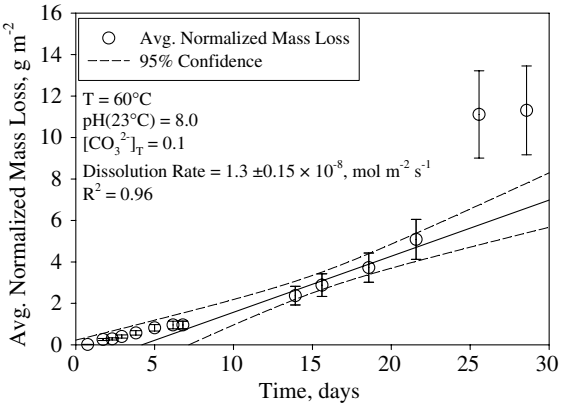

Fig. 11. Determination of the static dissolution rate.

in the static tests, the dissolution rate decreased. The chemical affinity computed with respect to the mineral rutherfordine (UO_2CO_3), $A = -7.1$ kJ mol^{-1}, using EQ3NR [45], for the static experiments was approximately four times greater than the chemical affinity computed for the SPFT test at the maximum dissolution rate [$\log_{10}(q/S) = -6.4$], $A = -26.7$ kJ mol^{-1}. This observation suggests static-test results were being affected by solubility constraints and highlights the importance of using the more applicable flow-through system for conducting dissolution experiments on UO_2. Therefore, the SPFT technique is preferred for kinetic rate law parameter measurements because it typically maintains constant solution chemistry.

In addition to flow rate, pH, and the static test, additional experiments were conducted as a function of bicarbonate to compare the results obtained in this study to those from previous investigators.

3.9. Comparison to previous results

Fig. 12 shows the dissolution rate for the calcined UO_2 powdered specimens at 30 °C, $q = 120$ mL d^{-1}, pH 8.0, and a $[CO_3^{2-}]_T$ of 0.001, 0.05, and 0.1 M. The solution ionic strength (I) was maintained at 0.1 M by adding 0.05 and 0.099 M of NaCl to the 0.05 and 0.001 M $[CO_3^{2-}]_T$ solutions, respectively. Using Eq. (7), a non-linear regression was performed on the entire data set, and the resulting regression coefficients were $k_0 = 9.1 \pm 3.2 \times 10^{-7}$ (mol m^{-2} s^{-1}) and $\eta_{[CO_3^{2-}]_T} = 1.3 \pm 0.1$ with a correlation coefficient (R^2) of 0.97. The forward rate constant and power law coefficients are different than those measured by Pablo et al. [23] at 45 °C ($k_0 = 8.7 \pm 0.52 \times 10^{-8}$ mol m^{-2} s^{-1}, $\eta_{[CO_3^{2-}]_T} = 0.98 \pm 0.02$).

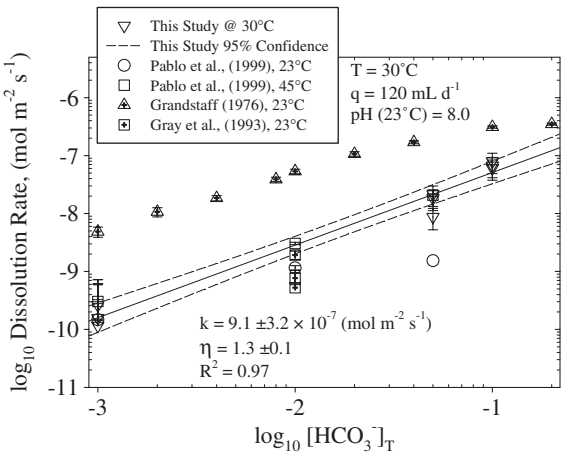

Fig. 12. Dissolution rate as a function of $[CO_3^{2-}]_T$. Comparison of the results from this study to previous studies.

The results obtained by previous investigators [11,20,23], normalized using the geometric surface area, are compared to our results in Fig. 12. The steady-state dissolution rates from this study correlate well with the rates of previous studies, with the exception of Grandstaff's [11] results, and suggest the mechanism of UO_2 dissolution is the same. The reason for the discrepancy in Grandstaff's [11] results is because the natural sample used contained a larger weight percent of U(VI), ~60% as UO_3, to U(IV), ~30% as UO_2, in comparison to the synthetic UO_2 samples used in other studies.

4. Conclusion

The experimental data presented in this study have added to our understanding of the reactions affecting UO_2 dissolution under dilute and near-saturated conditions, although more information is needed to accurately determine the rate-limiting step in the dissolution reaction. These results highlight the importance of specific surface area, solution saturation state, and pH in determining the dissolution rate of UO_2. Finally, results from static dissolution tests provided evidence that, in previous studies, the use of the static experimental method may have resulted in observed UO_2 dissolution rates that are lower than the forward or maximum dissolution rate. This reduction in the dissolution rate occurs because of changes in the chemical affinity, and therefore provides further evidence of the importance of understanding the role of solution saturation state on the dissolution of UO_2.

The information gathered in this study has provided some fundamental data necessary to determine the applicability of Redox permeable reactive barriers for the remediation of uranium contamination. These results illustrate uranium release, from UO_2 immobilized in the near-field of a Redox permeable reactive barriers, will be controlled by pH, solution saturation state, and the concentration of dissolved carbonate. Based on natural uranium sandstone deposits, it is believed that a rapid uranium release may result in the formation of secondary uranium minerals depending on the groundwater solution chemistry. These secondary minerals may eventually control the dissolved uranium concentration. However, to evaluate the effect of competing factors on uranium release, information on the effect of various complexing and/or inhibitor groundwater solution species are needed.

Acknowledgements

We would like to thank the following individuals; W.J. Martin, D.M. Wellman, L.R. Reed, S.V. Mattigod, K.M. Krupka, P.F. Martin, C.F. Brown, M.J. Lindberg,

B.W. Arey, D.D. Dauble, and G.P. O'Connor, of Pacific Northwest National Laboratory (PNNL) for their help and support in the preparation of this manuscript. I would also like to thank A.J. Englande of Tulane University for his guidance over the years. This research was supported by a grant from the National Physical Science Consortium in conjunction with PNNL and Tulane University (Pierce) and a DOE-EMSP grant FG07-99ER15022 (Catalano). PNNL and SSRL are supported by the US Department of Energy, Office of Basic Energy Sciences and Office of Biological and Environmental Research.

References

[1] A. Abdelouas, W. Lutze, H.E. Nuttall, et al., Comp. Ren. De L Acad. Des Sci. Serie II Fasc. A-Sci. De La Terr. et Des Planetes 328 (1999) 315.
[2] A. Abdelouas, Y. Lu, W. Lutze, et al., J. Contam. Hydrol. 35 (1998) 217.
[3] J.E. Szecsody, K.J. Cantrell, K.M. Krupka, et al., Pacific Northwest National Laboratory, PNNL-12048, 1998.
[4] M.D. Williams, V.R. Vermeul, J.E. Szecsody, et al., Pacific Northwest National Laboratory, PNNL-12153, 1999.
[5] J.S. Fruchter, J.E. Amonette, C.R. Cole, et al., Pacific Northwest National Laboratory, PNNL-11372 UC-602, 1996.
[6] M.D. Williams, V.R. Vermeul, J.E. Szecsody, et al., Pacific Northwest National Laboratory, PNNL-13349, 2000.
[7] J.K. Fredrickson, J.M. Zachara, D.W. Kennedy, et al., Geochim. Cosmochim. Acta 64 (2000) 3085.
[8] Y.A. Gorby, D.R. Loveley, Environ. Sci. Technol. 26 (1992) 205.
[9] J.N. Fiedor, W.D. Bostick, R.J. Jarabek, et al., Environ. Sci. Technol. 32 (1998) 1466.
[10] W.E. Schortman, M.A. Desea, Proceedings of the 2nd International United Nations Conference: Peaceful Uses of Atomic Energy, vol. 3, 1958, p. 333.
[11] D.E. Grandstaff, Econ. Geol. 71 (1976) 1493.
[12] R. Wang, Y.B. Katayama, Nucl. Chem. Waste Manage. 3 (1982) 83.
[13] K. Ollila, Nuclear Waste Commission of Finnish Power Companies, YJT-85-02, 1985.
[14] K. Ollila, Nuclear Waste Commission of Finnish Power Companies, YJT-86-28, 1986.
[15] K. Ollila, Nuclear Waste Commission of Finnish Power Companies, YJT-88-04, 1988.
[16] K. Ollila, J. Nucl. Mater. 190 (1992) 70.
[17] J. Bruno, I. Casas, I. Puigdomenech, Radiochim. Acta 44 (1987) 11.
[18] I. Casas, J. Gimenez, M. Martin, et al., Radiochim. Acta 66&67 (1994) 23.
[19] J. Posey-Dowty, E. Axtmann, D. Crerar, et al., Econ. Geol. 82 (1987) 184.
[20] W.J. Gray, J.C. Tait, S.A. Steward, et al., High Level Radioactive Waste Management, La Grange Park, IL, 1994, p. 2597.
[21] W.J. Gray, C.N. Wilson, Pacific Northwest National Laboratory, PNL-10540, 1995.
[22] M.E. Torrero, E. Baraj, J.D. Pablo, et al., Int. J. Chem. Kinet. 29 (1997) 261.
[23] J.D. Pablo, I. Casas, J. Gimenez, et al., Geochim. Cosmochim. Acta 63 (1999) 3097.
[24] B. Grambow, Swedish Nuclear Fuel and Waste Management Co., SKB-TR-89-13, 1989.
[25] D.W. Shoesmith, J. Nucl. Mater. 282 (2000) 1.
[26] J. Bruno, I. Casas, I. Puigdomenech, Geochim. Cosmochim. Acta 55 (1990) 647.
[27] R. Wang, Pacific Northwest Laboratory, PNL-3566, 1980.
[28] S. Sunder, J. Electroanal. Chem 0 (1981) 163.
[29] S. Sunder, J. Electroanal. Chem 150 (1983) 217.
[30] D.W. Shoesmith, S. Sunder, M.G. Bailey, et al., App. Surf. Sci. 20 (1984) 39.
[31] ASTM. American Society for Testing and Materials, ASTM C136, 2001.
[32] D.M. Strachan, H.T. Schaef, M.J. Schweiger, et al., Powder Diffr. 18 (2003) 23.
[33] G.E. Brown, G. Calas, G.A. Waychunas, et al., in: F.C. Hawthrone (Ed.), Spectroscopic Methods in Mineralogy and Geology, vol. 18, Mineralogy Society of America, Washington, DC, 1988.
[34] J.R. Bargar, G.E. Brown, I. Evans, et al., in: Proceedings of the Euroconference and NEA Workshop on Speciation, Techniques and Facilities for Radioactive Materials at Synchrotron Light Sources, Paris, France, 2002, p. 57.
[35] F.W. Lytle, R.B. Greegor, D.R. Sandstrom, et al., Nucl. Instr. Methods Phys. Res. Sec. A 226 (1984) 542.
[36] S.M. Webb, Phys. Scripta, in press.
[37] M. Newville, J. Sync. Rad. 8 (2001) 322.
[38] B. Wasserstein, Nature 174 (1954) 1004.
[39] A.L. Ankudinov, J.J. Rehr, Phy. Rev. B 56 (1997) R1712.
[40] G.R. Holdren, P.M. Speyer, Geochim. Cosmochim. Acta 51 (1987) 2311.
[41] L. Chou, R. Wollast, Geochim. Cosmochim. Acta 48 (1984) 2205.
[42] S.A. Carroll, J. Bruno, Radiochim. Acta 52&53 (1991) 187.
[43] B.P. McGrail, J.P. Icenhower, P.F. Martin, et al., Pacific Northwest National Laboratory, PNNL-13381, 2000.
[44] Chemchek, Chemchek Instruments, Inc., Richland, WA 99352, 1993.
[45] T.J. Wolery, LLNL, UCRL-MA-110662 PT III, 1992.
[46] J.C. Miller, J.N. Miller, Statistics for Analytical Chemistry, 2nd Ed., Ellis Horwood Limited, West Sussex, England, 1988.
[47] J. Petiau, G. Calas, D. Petitmaire, A. Bianconi, M. Benfatto, A. Marcelli, Phys. Rev. B 34 (1986) 7350.
[48] F. Farges, C.W. Ponader, G. Calas, et al., Geochim. Cosmochim. Acta 56 (1992) 4205.
[49] E.A.J.J.R. Hudson, J.J. Bucher, Phys. Rev. B 52 (1995) 13815.
[50] P.M. Bertsch, D.B. Hunter, Environ. Sci. Technol. 28 (1994) 980.
[51] D.K. Smith, in: F. Ippolito, B. DeVero, G. Capaldi (Eds.), Uranium Geochemistry, Mineralogy, Geology, Exploration, and Resources, Institution of Mining and Metallurgy, London, 1984.
[52] E.I. Sergeyeva, A.A. Nikitin, I.L. Khodakovkiy, et al., Geochem. Int. 9 (1972) 900.
[53] D. Langmuir, Geochim. Cosmochim. Acta 42 (1978) 547.
[54] A.K. Alwan, P.A. Williams, Miner. Mag. 43 (1980) 665.

[55] P.A.G. O'Hare, B.M. Lewis, S.N. Nguyen, J. Chem. Thermodyn. 20 (1988) 1287.
[56] P.A.G. O'Hare, J. Boerio, H.R. Hoekstra, J. Chem. Thermodyn. 8 (1976) 845.
[57] R. Vochten, L.V. Haverbeke, Contrib. Miner. Petrol. 43 (1990) 65.
[58] S.N. Nguyen, R.J. Silva, H.C. Weed, et al., J. Chem. Thermodyn. 24 (1992) 359.
[59] I. Grenthe, J. Fuger, R.J.M. Konings, et al., Chemical Thermodynamics of Uranium, Elsevier Science Publishers B.V., North-Holland, 1992.
[60] R.J. Finch, Mater. Res. Symp. Proc. 465 (1997) 1185.
[61] S.N. Kalmykov, G.R. Choppin, Radiochim. Acta 88 (2000) 603.
[62] F. Chen, R.C. Ewing, S.B. Clark, Am. Miner. 84 (1999) 650.
[63] R. Guillaumont, T. Fanghanel, V. Neck, et al., Update on the Chemical Thermodynamics of Uranium, Neptunium, Plutonium, Americium, and Technetium, Elsevier B.V., Amsterdam, The Netherlands, 2003.
[64] A.C. Lasaga, in: A.F. White, S.L. Brantley (Eds.), Chemical Weathering Rates of Silicate Minerals, vol. 31, Mineralogical Society of America, Washington, DC, 1995.
[65] H.C. Helgeson, W.M. Murphy, P. Aagaard, Geochim. Cosmochim. Acta 48 (1984) 2405.
[66] B.P. McGrail, W.L. Ebert, A.J. Bakel, et al., J. Nucl. Mater. 249 (1997) 175.